Implementation of the CIP as the Advection Solver in the MM5

XINDONG PENG

Earth Simulator Center, Yokohama, Japan

FENG XIAO AND TAKASHI YABE

Tokyo Institute of Technology, Tokyo, Japan

KEIJI TANI

Earth Simulator Center, Yokohama, Japan

(Manuscript received 25 May 2002, in final form 23 September 2002)

ABSTRACT

A semi-Lagrangian-type advection scheme, cubic-interpolated pseudoparticle (CIP) method is implemented to the fifth-generation Pennsylvania State University–NCAR Mesoscale Model (MM5, version 3.4). A dimensional splitting CIP algorithm, with spatial third-order and temporal second-order accuracy, is derived to compute the advection in the MM5. The modified model is evaluated with ideal tests and real case studies in comparing with the leapfrog scheme, which was originally employed in the MM5. The CIP method appears remarkably superior to the leapfrog scheme in respect to both dissipative and dispersive errors, especially when discontinuities or large gradients exist in the advected quantity. Two real cases of severe mesoscale phenomena were simulated by using both the CIP scheme and the leapfrog scheme. In the advection dominant regions, the CIP shows remarkable advantages in capturing the detail structures of the predicted field. As computations with high resolution become more and more popular in experimental and/or operational modeling, implementing more accurate advection in numerical models, as is done in the present study, will be increasingly demanded.

1. Introduction

Advection, as a basic process, plays an important role in fluid dynamics. It must be accurately represented in numerical models for correct predictions of various weather phenomena. The improvement of the predictions for many meso- or synoptic-scale systems, such as cloud convection, squall lines, or cold fronts, relies heavily on how to treat the advection numerically. As a matter of fact, these advection-dominant weather systems are far from being well predicted in current numerical models. There are many aspects of the existing numerical models that need to be improved, including both the dynamic framework and the physical package. For migratory weather systems, the advection calculation is worthy of more attention before tuning the parameterizations to get better simulation results. However, there is still room for improving the advection computation in many numerical models. Furthermore, the numerical errors from advection computation become more and more significant as the resolution of the numerical simulation becomes increasingly refined. Thus, incorporating some sophisticated advection schemes into the existing models can be a step toward more accurate simulations.

Numerical advection has been intensively investigated in almost all fields related to computational fluid dynamics in the past decades. Many numerical schemes have been designed so far with an emphasis on different numerical properties, such as dissipation, dispersion, conservation, and shape preservation. A class of so-called high-resolution schemes has been developed for hyperbolic conservation laws in aerodynamic simulations. These types of schemes are basically Eulerian in nature and use the flux formulation to assure the conservation of the transported quantity, which proved to be essential for obtaining the correct weak solutions to the nonlinear discontinuous (shock waves). Some representatives of the Eulerian high-resolution schemes include the Total Variation Diminishing (TVD) scheme (Harten 1983), the Monotonic Upstream-centered Scheme for Conservation Lows (MUSCL) scheme (van Leer 1977, 1979), and the Piecewise Parabolic Method (PPM) scheme (Colella and Woodward 1984). Applications of Eulerian high-resolution schemes to atmo-

Corresponding author address: Dr. Xindong Peng, Earth Simulator Center, 3173-25 Showamachi, Kanazawa-ku, Yokohama, Kanagawa 236-0001, Japan.
E-mail: peng@es.jamstec.go.jp

spheric dynamics have been reported in the literature (Carpenter et al. 1990). On the other hand, semi-Lagrangian-type schemes have been developed and widely used in meteorological simulations. Staniforth and Côté (1991) give a good review of semi-Lagrangian schemes and their implementations in atmospheric models.

Being a semi-Lagrangian-type method, the CIP scheme has been developed to compute the advection by Yabe and his coworkers (Yabe and Aoki 1991; Yabe et al. 1991). The cubic-interpolated pseudo particle (CIP) method is unique in that it introduces an extra ''moment,'' the gradient of the dependent variable. Both the dependent variable and its gradient are predicted according to the Lagrangian invariant solutions of the advection equation. The CIP uses a cubic interpolation, but requires only information on the variable and its spatial gradient of just one grid cell to construct the interpolating polynomial and needs no more operation counts than the conventional semi-Lagrangian scheme based on cubic Lagrangian interpolation or on a cubic spline. Being completely explicit and with compact spatial stencils, the CIP method is parallelization oriented. By making use of the Lagrangian solution to the advected quantity and its gradient moment, the CIP gives high accuracy in numerical dispersion, and is able to satisfactorily capture discontinuity or a large gradient. So far, the scheme has been widely applied to general fluid dynamics and various multiphase fluid simulations (see Yabe et al. 2001 for a review of the method), but not yet been used in a meteorological model.

With the rapid growth in the power of computer hardware, the peak speed of the fastest computer available for meteorological simulation approaches several tens of TFLOPS, for example, the Earth Simulator supercomputer system recently installed in Japan (details available online at http://www.es.jamstec.go.jp). It is possible to run meteorological models with extremely fine spatial resolution. For example, a rough estimation shows that a regional model can use a grid spacing of several hundred meters. With such a resolution, clouds and turbulent eddies may to a large extent be explicitly resolvable. The transportation and exchange of water substance or other physical quantities needs to be directly computed by solving advection equation. Another problem associating with the highly refined computational grid is that the discontinuities or large jumps in dependent variables will become quite significant. Therefore, the effects from the advection computation will be more striking than ever before. As an attempt to improve the advection computation, we have incorporated the CIP method into the fifth-generation Pennsylvania State University–National Center for Atmospheric Research (Penn State–NCAR) Mesoscale Model (MM5). Considering multidimensional implementation, we used the primary version of the CIP (Yabe and Aoki 1991; Yabe et al. 1991), which appears to be good in accuracy and dispersion property even though it is not one of the conservative schemes described in Tanaka et al. (1999) and Yabe et al. (2001).

The MM5 (Dudhia 1993) is one of the most well known and popular meteorological mesoscale models, and has been applied to research and forecasting of mesoscale phenomena by a wide spectrum of users. Nonhydrostatic equations for a fully compressible atmosphere in a rotating frame of reference are adopted in this model. It has a σ vertical coordinate system and many options for parameterizations of various physical processes. However, on the advection, only the central spatial difference on a B grid with the leapfrog-type temporal integration (hereinafter referred to as leapfrog) scheme is available in the model. In model dynamics, the use of a rigid upper boundary condition eliminates external gravity waves. For the sound waves that exist in the compressible model atmosphere, a split time step approach is utilized in the model to treat the acoustic waves semi-implicitly with a shorter time step. Other relatively ''fast modes,'' like internal gravity waves, are also permitted in the model. In the modified model presented in this paper, the time step limit for the computational stability regarding the advection is relaxed by replacing the leapfrog with the CIP. In the whole model, however, the fast modes still prevent a large increase in the time step. Since the nonadvection parts remain as they are in the original model, the largest permissible Courant–Friedrichs–Lewy (CFL) number for the modified model was not pursued and all the experiments were carried out with CFL numbers of less than unity.

In this paper, as a preliminary effort to modify the existing models for more accurate advection calculation, we will discuss the application of the CIP to the MM5 (version 3.4). In section 2, we show the algorithm of the CIP and its implementation in MM5. Section 3 presents numerical experiments including pure advection tests and real case studies with emphasis on the comparisons between the CIP and the leapfrog. Finally, the major conclusions are given in section 4.

2. Implementation of the CIP to MM5

a. The model equations for the CIP method

As mentioned in the above section, the CIP method introduces the gradient of the transported quantity as an extra moment that is predicted by another prognostic equation. The target equations for the CIP is a set of linked equations with both the advected physical variable and its gradient moment(s) being the prognostic quantities.

Consider the 1D advection equation in a form as

$$\frac{\partial F}{\partial t} + u\frac{\partial F}{\partial x} = 0, \tag{1}$$

with u being the advective velocity and F the transported

variable. In addition to computing F with (1), the CIP method also solves the accompanying equation,

$$\frac{\partial F_x}{\partial t} + u\frac{\partial F_x}{\partial x} = -\frac{\partial u}{\partial x}\frac{\partial F_x}{\partial x}, \tag{2}$$

to advance the gradient $F_x = \partial F/\partial x$.

The 2D schemes can be similarly designed by solving the following equations:

$$\frac{\partial F}{\partial t} + u\frac{\partial F}{\partial x} + v\frac{\partial F}{\partial y} = 0, \tag{3}$$

$$\frac{\partial F_x}{\partial t} + u\frac{\partial F_x}{\partial x} + v\frac{\partial F_x}{\partial y} = -F_x\frac{\partial u}{\partial x} - F_y\frac{\partial v}{\partial x}, \quad \text{and} \tag{4}$$

$$\frac{\partial F_y}{\partial t} + u\frac{\partial F_y}{\partial x} + v\frac{\partial F_y}{\partial y} = -F_x\frac{\partial u}{\partial y} - F_y\frac{\partial v}{\partial y}. \tag{5}$$

As shown later, the cubic polynomial interpolation function in 1D is constructed by using F and F_x, while the 2D construction is based on F, F_x, and F_y. The readers are referred Yabe and Aoki (1991) and Yabe et al. (1991) for details of the scheme.

In order to incorporate the CIP method into the MM5 model where the advection computation is calculated in a different formulation, we need to modify the prognostic equations in MM5. The following subsections describe how to recast the model equations in MM5 and how to apply CIP for the advection computation.

b. Modification of MM5 equations

In the MM5, the advection computation for all prognostic variables is written in flux form and discretized by a central differencing. In order to accommodate the MM5 to the CIP method, we need to modify the advection-related part of the governing equations from the flux form into an advective form.

Let F represent any variable of u, v, w, T, p', q_v or the microphysical variables in the MM5; then the original model equation can be generally written as

$$\frac{\partial p^*F}{\partial t} = -m^2\left(\frac{\partial p^*uF/m}{\partial x} + \frac{\partial p^*vF/m}{\partial y}\right) - \frac{\partial p^*F\dot{\sigma}}{\partial \sigma} + F(\mathrm{DIV}) + p^*G, \tag{6}$$

where

$$\mathrm{DIV} = m^2\left(\frac{\partial p^*u/m}{\partial x} + \frac{\partial p^*v/m}{\partial y}\right) + \frac{\partial p^*\dot{\sigma}}{\partial \sigma}$$

and p^*G represents all the nonadvection terms. See Dudhia (1993) for all the denotations in (6).

It should be noted that the vertical coordinate σ in the present nonhydrostatic model is defined according to the *reference-state* pressure p_0. The surface pressure of the reference-state atmosphere (p_{surf}) is constant with time. As p_{top} is also a constant, it follows that $p^* = p_{\mathrm{surf}} - p_{\mathrm{top}}$ is constant with time and depends only upon the terrain altitude and, thus, upon x and y only. Considering

$$\frac{\partial p^*F}{\partial t} = p^*\frac{\partial F}{\partial t},$$

Eq. (6) can be rewritten as

$$p^*\frac{\partial F}{\partial t} = -p^*\left(mu\frac{\partial F}{\partial x} + mv\frac{\partial F}{\partial y} + \dot{\sigma}\frac{\partial F}{\partial \sigma}\right) + p^*G.$$

Therefore, we get a set of prognostic equations in advective form as

$$\frac{\partial F}{\partial t} = -U\frac{\partial F}{\partial x} - V\frac{\partial F}{\partial y} - \dot{\sigma}\frac{\partial F}{\partial \sigma} + G, \tag{7}$$

where $U = mu$ and $V = mv$.

The CIP method can be immediately used to solve all the governing equations expressed as (7). The extra prognostic equations for the gradient moments can be simply derived by differentiating (7) with respect to x, y, and σ separately. Thus, we end up with the equations for F_x, F_y, and F_σ as

$$\frac{\partial F_x}{\partial t} = -U\frac{\partial F_x}{\partial x} - V\frac{\partial F_x}{\partial y} + \frac{\partial G}{\partial x} - F_x\frac{\partial U}{\partial x} - F_y\frac{\partial V}{\partial x} - \frac{\partial \dot{\sigma}F_\sigma}{\partial x}, \tag{8}$$

$$\frac{\partial F_y}{\partial t} = -U\frac{\partial F_y}{\partial x} - V\frac{\partial F_y}{\partial y} + \frac{\partial G}{\partial x} - F_x\frac{\partial U}{\partial y} - F_y\frac{\partial V}{\partial y} - \frac{\partial \dot{\sigma}F_\sigma}{\partial y}, \tag{9}$$

$$\frac{\partial F_\sigma}{\partial t} = -\dot{\sigma}\frac{\partial F_\sigma}{\partial \sigma} + \frac{\partial G}{\partial \sigma} - \frac{\partial UF_x}{\partial \sigma} - \frac{\partial VF_y}{\partial \sigma} - F_\sigma\frac{\partial \dot{\sigma}}{\partial \sigma}. \tag{10}$$

Splitting (7) into vertical and horizontal directions and rearranging the above equations, we can get other sets of governing equations for the following parts:

horizontal advection part,

$$\frac{\partial F}{\partial t} = -U\frac{\partial F}{\partial x} - V\frac{\partial F}{\partial y}, \tag{11}$$

$$\frac{\partial F_x}{\partial t} = -U\frac{\partial F_x}{\partial x} - V\frac{\partial F_x}{\partial y} - F_x\frac{\partial U}{\partial x} - F_y\frac{\partial V}{\partial x}, \tag{12}$$

$$\frac{\partial F_y}{\partial t} = -U\frac{\partial F_y}{\partial x} - V\frac{\partial F_y}{\partial y} - F_x\frac{\partial U}{\partial y} - F_y\frac{\partial V}{\partial y}; \tag{13}$$

vertical advection part,

$$\frac{\partial F}{\partial t} = -\dot{\sigma}\frac{\partial F}{\partial \sigma}, \tag{14}$$

$$\frac{\partial F_\sigma}{\partial t} = -\dot{\sigma}\frac{\partial F_\sigma}{\partial \sigma} - F_\sigma\frac{\partial \dot{\sigma}}{\partial \sigma}; \quad \text{and} \tag{15}$$

nonadvection part

$$\frac{\partial F}{\partial t} = G, \tag{16}$$

$$\frac{\partial F_x}{\partial t} = \frac{\partial G}{\partial x} - \frac{\partial \dot{\sigma} F_\sigma}{\partial x}, \tag{17}$$

$$\frac{\partial F_y}{\partial t} = \frac{\partial G}{\partial x} - \frac{\partial \dot{\sigma} F_\sigma}{\partial y}, \tag{18}$$

$$\frac{\partial F_\sigma}{\partial t} = \frac{\partial G}{\partial \sigma} - \frac{\partial U F_x}{\partial \sigma} - \frac{\partial V F_y}{\partial \sigma}. \tag{19}$$

Leaving the leapfrog time integration formulation unchanged, we introduce these procedures into MM5 by separating the time tendency into the advection and the nonadvection parts. All packages except the advection then can also be used in the modified model without any change.

c. Advection computation by CIP

Though a fully three-dimensional CIP method (Yabe et al. 1991) is available, we adopt a spatial splitting CIP method in MM5, as a combination of a vertical 1D and a horizontal 2D scheme. The vertical advection is computed separately from the horizontal one, so that it can be consistent with the cumulus convective parameterization options in the model. For example, the Kuo–Anthes scheme (Anthes 1977) describes a final state of vertical convection; there is no need to calculate vertical advection after convective parameterization. However, the vertical advection needs to be explicitly calculated for any other convective parameterization scheme installed in the model. Separately computing the vertical advection provides us the flexibility or convenience to switch among different parameterization schemes. This horizontal–vertical (HV) splitting algorithm, which implements the asynchronous computations of horizontal and vertical advections as expressed by (11)–(13) and (14) and (15), will be described as the following.

1) HORIZONTAL ADVECTION COMPUTATION WITH 2D CIP

First, let us deal with the horizontal advection part as expressed by (11)–(13) with a leapfrog-type integration. The CIP method makes use of the Lagrangian invariant solution for the advection parts of the above equations as

$$F(\mathbf{X}, t + \Delta t) = F(\mathbf{X} - \hat{\mathbf{X}}, t - \Delta t), \tag{20}$$

$$F_x(\mathbf{X}, t + \Delta t) = F_x(\mathbf{X} - \hat{\mathbf{X}}, t - \Delta t), \quad \text{and} \tag{21}$$

$$F_y(\mathbf{X}, t + \Delta t) = F_y(\mathbf{X} - \hat{\mathbf{X}}, t - \Delta t), \tag{22}$$

where $\mathbf{X}$ is the position of any Eulerian grid point and $\hat{\mathbf{X}}$ is the distance a particle travels in time increment $2\Delta t$ during $[t - \Delta t, t + \Delta t]$ and is the solution of the following initial value problem:

$$\frac{d\mathbf{X}_1}{dt_1} = \mathbf{U}(\mathbf{X} - \mathbf{X}_1, t_1), \tag{23}$$

$$\mathbf{X}_1|_{t_1 = t - \Delta t} = 0. \tag{24}$$

Though the trajectory $\mathbf{U}$ varies with time during $[t - \Delta t, t + \Delta t]$, in the present study, the displacement $\hat{\mathbf{X}}$ is simply estimated by using the velocity field $\mathbf{U} = (U, V)$ defined on the computational grid points at time t,

$$\hat{\mathbf{X}} = 2\mathbf{U}(\mathbf{X}, t)\Delta t, \tag{25}$$

and a second-order temporal precision is achieved.

As in other conventional semi-Lagrangian schemes, the CIP method needs to interpolate a profile for the advected quantity to find the solution at the departure point $(\mathbf{X} - \hat{\mathbf{X}})$ that does not coincide with any grid point. In this study, we use a piecewise cubic polynomial:

$$\overline{F}^{2D}(x, y) = a_1X^3 + a_2X^2Y + a_3XY^2 + a_4Y^3 + a_5X^2 + a_6XY + a_7Y^2 + a_8X + a_9Y + a_{10} \tag{26}$$

for grid cell $[x_{i,j}, x_{\text{inu},j}] \times [y_{i,j}, y_{i,\text{jnu}}]$, where the subscript inu and jnu show the indices of the upstream neighboring grid points of $(x_{i,j}, y_{i,j})$ in the x and y directions, respectively, and $X = x - x_{i,j}$, $Y = y - y_{i,j}$. Given the values of F, F_x, and F_y at (i, j), (inu, j), and (i, jnu), and the values of F at (inu, jnu), we can completely determine the coefficients a_1 to a_{10} in (26) (refer to Yabe et al. 1991 for details).

Consequently, the interpolation functions for the gradient moments read

$$\overline{F}_x^{2D}(x, y) = 3a_1X^2 + 2a_2XY + a_3Y^2 + 2a_5X + a_6Y + a_8, \tag{27}$$

$$\overline{F}_y^{2D}(x, y) = a_2X^2 + 2a_3XY + 3a_4Y^2 + a_6X + 2a_7Y + a_9. \tag{28}$$

From the Lagrangian invariant solutions (20)–(22), F, F_x, and F_y are predicted by substituting $X = -U\Delta t$ and $Y = -V\Delta t$ into (26)–(28). According to (12) and (13), the Lagrangian invariant solutions for F_x and F_y are further corrected due to the terms $-F_x\partial U/\partial x - F_y\partial V/\partial x$ and $-F_x\partial U/\partial y - F_y\partial V/\partial y$, respectively.

2) VERTICAL ADVECTION COMPUTATION WITH 1D CIP

In order to get the semi-Lagrangian solution for the vertical advection part, that is, Eqs. (14) and (15), we use a cubic polynomial interpolation, such as

$$\overline{F}^{1D}(\sigma) = b_1Z^3 + b_2Z^2 + b_3Z + b_4, \tag{29}$$

for any grid cell $[\sigma_k, \sigma_{\text{knu}}]$. The subscript knu shows the index of the grid point next to σ_k in the upstream direction, and $Z = \sigma - \sigma_k$. Thus, the interpolation function for the gradient moment with respect to σ is

$$\overline{F}_{\sigma}^{1D}(\sigma) = 3b_1Z^2 + 2b_2Z + b_3. \quad (30)$$

Given F and F_σ at σ_k and σ_{knu}, we can determine the four coefficients b_1, b_2, b_3, and b_4 in (29) (Yabe and Aoki 1991; Yabe et al. 2001). As long as the interpolation function is constructed, the Lagrangian invariant solutions to F and F_σ are computed by replacing Z with $-\dot{\sigma}\Delta t$ in (29) and (30).

Since the gradient moment of the vertical advection is subject to the divergence correction as shown by Eq. (15), a modification to the Lagrangian invariant solution of F_σ due to the divergence term, $-F_\sigma\partial\dot{\sigma}/\partial\sigma$, needs to be computed.

d. Computation of the nonadvection part

Since we adopted a fractional step approach, the nonadvection part, shown as (16)–(19), can be easily computed. We solve (16) by using the existing routines in the original MM5 model for all the dynamical and physical processes except the advection. All the physics processes are computed as they are in the original model after the advection is solved. As shown in the next subsection, with the temporal tendency G for the nonadvection part known, we can get the spatial differential terms in (17)–(19) by simply using a central differencing.

e. Summary of the solution procedures

By recasting the advection equation into advective form, we have modified the MM5 and incorporated the CIP method as the advection solver. We retained the leapfrog-type time integration algorithm in the original model. The updating of any prognostic variable from step $\tau - 1$ to step $\tau + 1$ is conducted by using the time tendency computed at step τ, such as

$$F^{\tau+1} = F^{\tau-1} + 2\Delta t\left(\frac{\partial F}{\partial t}\right)^{\tau}.$$

The time tendency from the advection at step τ is obtained by the CIP method, while all tendency computations for the nonadvection parts remain as they are in the original model. Because the time tendency is not available for the starting step, an Euler forward type temporal integration is used at the first step; that is,

$$F^{1} = F^{0} + \Delta t\left(\frac{\partial F}{\partial t}\right)^{0}.$$

The numerical procedure for updating a prognostic variable in the modified MM5 includes the following steps:

1) From the initial condition of F^0, compute F_x^0, F_y^0, and F_σ^0 with the central differencing method.
2) Call 2D and 1D solvers to predict F^1, F_x^1, F_y^1, and F_σ^1, which are updated with nonconvective tendency. In detail, the following procedure, that is, steps 3–7, is followed to fulfill this task by simply replacing τ, $\tau - 1$ with 0, $\tau + 1$ with 1, and time increment $2\Delta t$ with Δt.

   For any $\tau \geq 2$, as shown in steps 3–7, we present a leapfrog time integration algorithm based on three time levels denoted as $\tau - 1$, τ and $\tau + 1$.
3) Call the 2D CIP solver to compute the horizontal advection, that is, Eqs. (11)–(13). Here, $F^{\tau-1}$, $F_x^{\tau-1}$, $F_y^{\tau-1}$, and U^τ, V^τ are used for the advection computation from $\tau - 1$ to $\tau + 1$ with the time integration interval of $t^{\tau+1} - t^{\tau-1} = 2\Delta t$. The advection velocity defined at the central point gives second-order accuracy. Let the results after the horizontal advection computed by the CIP be F^*, F_x^*, and F_y^*, and the corresponding time tendency in leapfrog style for step τ can be written as

$$\left(\frac{\partial F}{\partial t}\right)_{hadv}^{\tau} = \frac{F^* - F^{\tau-1}}{2\Delta t}.$$

4) Modify F_σ with F_x^* and F_y^* according to

$$F_\sigma^* = F_\sigma^{\tau-1} - 2\Delta t\left(\frac{\partial U^\tau F_x^*}{\partial\sigma} + \frac{\partial V^\tau F_y^*}{\partial\sigma}\right).$$

5) Call the 1D CIP solver to compute the vertical advection, that is, Eqs. (14) and (15), based on F^* and F_σ^*. The vertical velocity $\dot{\sigma}^\tau$ is used as the effective advection velocity. Intermediate results after the vertical advection are denoted by F^{**} and F_σ^{**}, and the time tendency for the vertical advection at step τ is similarly written as

$$\left(\frac{\partial F}{\partial t}\right)_{vadv}^{\tau} = \frac{F^{**} - F^*}{2\Delta t}.$$

6) Compute the nonadvective terms G^τ at time step τ (as in the original MM5), and then predict $F^{\tau+1}$ according to Eq. (7), that is,

$$F^{\tau+1} = F^{\tau-1} + 2\Delta t\left[\left(\frac{\partial F}{\partial t}\right)_{hadv}^{\tau} + \left(\frac{\partial F}{\partial t}\right)_{vadv}^{\tau} + G^\tau\right],$$

   to get the prognostic variable at $t = t^{\tau+1}$.
7) Finally, the gradient moments F_x^*, F_y^*, and F_σ^{**} are updated by

$$F_x^{\tau+1} = F_x^* + 2\Delta t\left(\frac{\partial G^\tau}{\partial x} - \frac{\partial\dot{\sigma}^\tau F_\sigma^{**}}{\partial x}\right),$$

$$F_y^{\tau+1} = F_y^* + 2\Delta t\left(\frac{\partial G^\tau}{\partial y} - \frac{\partial\dot{\sigma}^\tau F_\sigma^{**}}{\partial y}\right), \quad \text{and}$$

$$F_\sigma^{\tau+1} = F_\sigma^{**} + 2\Delta t\frac{\partial G^\tau}{\partial\sigma}.$$

8) Go back to step 3 for the next time step.

3. Numerical tests

a. Pure advection tests

To evaluate the CIP method and verify the modified MM5 code, we first tested the modified MM5 model with pure advection experiments. The HV splitting CIP scheme was tested in comparison with the original leapfrog advection scheme in the MM5. We designed three 2D ideal advection experiments with different initial conditions and one 3D experiment. All the physics processes were switched off for the pure advection tests. In all four of the advection tests, the initial distribution of variable F, which is actually defined as the water vapor mixing ratio in all the tests, was transported by a uniform wind field. In all the numerical experiments reported in this paper, if there is no special declaration, we retained the Asselin filter as it is in the original MM5.

1) INITIAL CONDITIONS

In order to evaluate the accuracy of the numerical schemes in computing advection with various resolutions and different gradients, initial distributions with different sizes and different spatial gradients are defined in the following for a domain of 500 × 500 grid points.

1) A smooth distribution of large size

$$F = \frac{1 + \cos(r\pi)}{2},$$

where

$$r = \min\left[1, 4\sqrt{\left(\frac{i - 125}{250}\right)^2 + \left(\frac{j - 125}{250}\right)^2}\right],$$

with i, j being the grid indices. It is a simple cosine wave with relatively long wavelength and should be well resolved by both of the numerical schemes.

2) A discontinuous distribution of large size,

$$F = \begin{cases} 1, & \text{for } 50 \le i, \quad j \le 100, \\ 0, & \text{others,} \end{cases}$$

which is a square wave covering large area. As we know, the square wave or a large gradient requires a wide spectrum of the Fourier modes to approximate; thus it is usually used to test the dispersion properties of a numerical scheme.

3) A discontinuous distribution of small size,

$$F = \begin{cases} 1, & \text{for } 53 \le i, \quad j \le 60, \\ 0, & \text{others.} \end{cases}$$

It is also a square wave, but covers a relatively small region. The initial distribution will be easily distorted if the numerical scheme has significant dispersion of dissipation errors.

The above three initial conditions are designed for the 2D tests. The initial conditions for the 3D test are defined on a 250 × 250 × 23 mesh as follows.

4) A discontinuous distribution of small size,

$$F = \begin{cases} 1, & \text{for } 7 \le i, \quad j \le 13 \quad \text{and} \quad 4 \le k \le 10, \\ 0, & \text{others;} \end{cases}$$

where k is the grid index in the vertical direction. Distribution 4 is basically the same as distribution 3, except that it is a 3D problem. It serves to verify the HV splitting in the 3D advection calculation.

The horizontal grid spacing is 10 km in all the tests; and the vertical domain is divided into 23 σ levels for test 4), which are located at 0.995, 0.985, 0.97, 0.945, 0.91, 0.87, 0.825, 0.775, 0.725, 0.675, 0.625, 0.575, 0.525, 0.475, 0.425, 0.375, 0.325, 0.275, 0.225, 0.175, 0.125, 0.075, and 0.025, respectively. In all of the experiments, $u = v = 12.5$ m s^{-1} is specified. In the 3D test a periodic velocity $\dot{\sigma}$ is specified in the vertical direction as

$$\dot{\sigma} = \begin{cases} 1.0 \times 10^{-5}, & \text{int}(\tau/40) = \text{even number}, \\ -1.0 \times 10^{-5}, & \text{int}(\tau/40) = \text{odd number}, \end{cases}$$

where τ represents the step number of the time integration. Vertical velocity changes its sign every 40 time steps, in order to avoid the influence from upper and lower boundaries. A small vertical velocity is selected so that the Courant number in the σ direction is not larger than that in the horizontal direction. In these pure advection experiments, a constant map projection factor is specified as $m = 1$ and the reference thickness of the model atmosphere is $p^* = 900$ hPa. All the nonadvective terms are switched off by setting $G = 0$. The Courant number is specified to be 0.5 (0.25) in all of the CIP (leapfrog) experiments. In all cases involving the leapfrog scheme, the Asselin filter, $\hat{F}^t = \mu F^t + \nu(F^{t+1} + \hat{F}^{t-1})$, is retained with weights of $\nu = 0.1$ and $\mu = 1 - 2\nu$ in the model.

2) RESULTS OF THE PURE ADVECTION TESTS

Since only the advection process is considered and a constant wind field is used in these ideal tests, the initial profiles should be transported downstream without deformation. First, 2D experiments were conducted by using the leapfrog and the CIP methods, respectively, with the initial distributions 1–3. The numerical results at 4000, 4667, and 5333 min are displayed in Fig. 1. The shaded areas in the panels show negative values, and the black boxes in Figs. 1e,f,h,i illustrate the exact solution of the advection corresponding to the different initial distributions. Labels on both axes mark a relative position in latitude and longitude.

In the experiment with smooth horizontal distribution, that is, initial condition 1 (Fig. 1a), both the leapfrog and the CIP methods provide satisfactory results. The initial profile was transported to the right position by

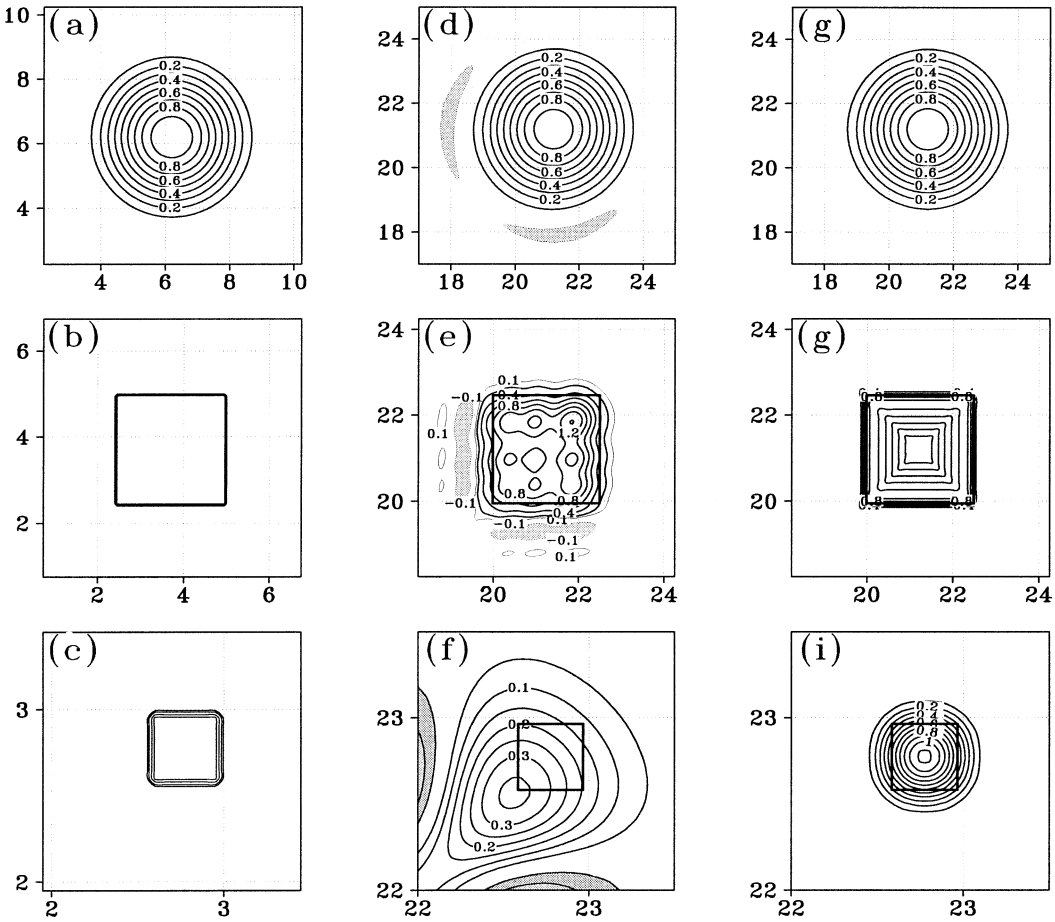

FIG. 1. Ideal advection test for the CIP and leapfrog schemes in expts 1, 2, and 3. Panels in left column are the initial conditions, middle-column panels are corresponding results of the leapfrog, while right column is that of the CIP.

both schemes without noticeable dissipation error, and the smearing in amplitude is quite small. However, it is obvious that the result of the leapfrog method is associated with more significant numerical oscillations (i.e., undershot) as shown in Fig. 1d. For a discontinuous distribution (Fig. 1b), the dispersion error of the leapfrog scheme becomes quite significant as shown in Fig. 1e. Spurious wave chains extend in the upstream directions along both the latitude and longitude. The amplitude of the numerical oscillations in the leapfrog scheme is much larger than that in the CIP scheme. Interference of the orthogonal computational waves heavily distorted the numerical transport. As a result, the overshot and undershot do not appear to be uniform (shown in Fig. 1e), and several local extreme centers formed around the discontinuous jump. On the other hand, as shown in Fig. 1h, this kind of error is negligibly small in the CIP scheme. For a distribution with a discontinuous jump and of small size (Fig. 1c), the superiority of the CIP method becomes much more significant. In this case, the numerical solution of the leapfrog method was largely deformed, as is illustrated in Fig. 1f. Numerical dispersions contaminated the numerical solution and gave poor results for the advection transport. The phase lag in displacement is also observed. The CIP method, on the other hand, gave a numerical solution that appears to be adequately accurate with respect to dissipative error, dispersive error, and distortion of the transported field.

A further comparison of the overshot and the undershot of the two schemes can be conducted by showing the time series of the maximum and the minimum values of the transported field. Figure 2 presents the time variations of the maximum and the minimum during the computations. With the same initial conditions, the oscillatory errors in the CIP are much less than those in the leapfrog. We find that the numerical oscillation from the leapfrog scheme depends on the smoothness of the initial distribution. A steeper distribution tends to cause larger numerical oscillations. Even in the case of a smooth distribution (i.e., initial data condition 1), the numerical oscillations of leapfrog have their amplitudes varied obviously as the integration time increases. On the contrary, both the overshot and the undershot in the

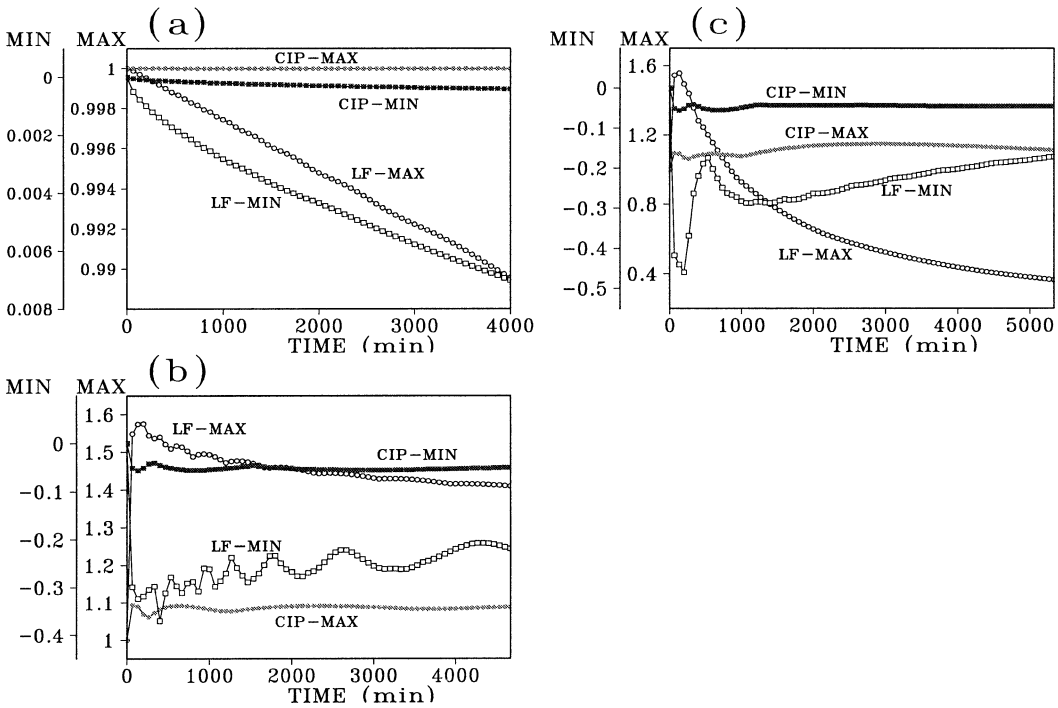

FIG. 2. Time series of the maximum and minimum in ideal tests of the CIP and leapfrog schemes with initial conditions 1, 2, and 3. The *y* axis labels to the left of the panels show the scales of the maximum and minimum; the *x* axis labels show the time in min.

result of the CIP method are very small, as shown in Fig. 2a. In the case of initial condition 2, which includes a large jump, both the overshot and the undershot from the leapfrog method are very large (Fig. 2b). The maximum gets to approximately 60% over the true solution, and the minimum reaches a 35% undershot. Although some tiny wiggles are observed in the results of the CIP scheme due to the cubic polynomial interpolation used in the scheme, the numerical oscillation in the CIP method is very local and appears only in the vicinity of discontinuity or a large jump. These oscillations do not grow with time. The spurious nonmonotonicity errors in the CIP method are less than 8%, even in the worst case, and can be easily controlled by modifying the interpolation function (Xiao et al. 1996). When applied to a distribution of small size but with large jump, that is, case 3, as shown in Fig. 1c, the leapfrog scheme gives rise to large dispersion errors and numerical oscillations, which leads such significant errors in the transported field that the numerical solution cannot be a physically meaningful one. The CIP method gets reasonable result (Fig. 2f) even for this difficult case.

With the increased resolution in the computational grid, more and more physics may to a large extent be directly computed in the meteorological models. There will be more detailed structures with a large gradient existing in the physical fields. The advection scheme should be able to capture these structures with an adequate accuracy. Our numerical experiments show the potential of the CIP for this purpose.

The 3D test was conducted with the initial distribution defined by case 4. The results after 2700 min are illustrated with the isosurface of 0.1 in Fig. 3. Similar to experiments 2 and 3, the CIP method gave an adequate numerical result with an accurate transport distance. The leapfrog scheme, however, is associated with significant dispersion error and numerical oscillations. The oscillations with large amplitudes spread over the whole computational domain. We should also note that a three-dimensional leapfrog scheme suffers a more restrictive Courant number than it does in two dimensions for computational stability. The CIP appears stable for a Courant number of less than one for all of the one-, two-, and three-dimensional computations. Actually, being semi-Lagrangian in type, the CIP method can be constructed to be free of the restriction in terms of Courant number for computational stability.

The above ideal tests show that the CIP method is much superior to the leapfrog advection scheme used in the MM5. Thus, improvement can be expected through the implementation of the CIP scheme. In particular, the capability of the CIP method to resolve the small structures with large gradients makes it attractive for high-resolution simulations. The result of the CIP in experiment 4 validated the splitting scheme used in the modified model.

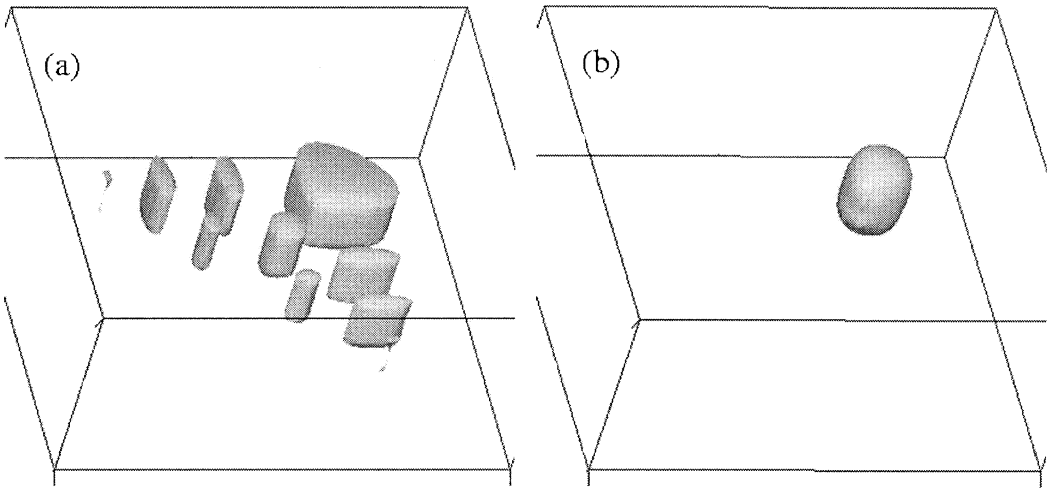

FIG. 3. Three-dimensional ideal advection result at 2700 min, by using the CIP and leapfrog schemes in experiment 4. Isogram surface of 0.1 is plotted for (a) the leapfrog and (b) the CIP.

3) A FEW REMARKS ON COMPUTATIONAL COST AND STABILITY

The CIP method requires almost the same operation counts as any conventional semi-Lagrangian scheme using cubic Hermite interpolation. The reconstruction of the high-order interpolation function is computationally heavier than the simple central differencing used in the leapfrog scheme. Nevertheless, at least two major advantages make the CIP scheme attractive. The first is that high accuracy in spatial approximation can be obtained with the CIP interpolation reconstruction, and the numerical dispersion errors are quite small. Second, regarding the pure advection computation, a CIP scheme can actually be designed to allow a large time integration step, as in any other semi-Lagrangian method.

However, the stable CFL number for the leapfrog scheme is restrictively limited, especially in the multidimensional case. A simple stability analysis for the linear advection problem shows that the necessary conditions for the leapfrog scheme to be stable are CFL $\leq$ 1 for 1D, CFL $\leq$ 1/2 for 2D, and CFL $\leq$ 1/3 for 3D. This can be easily confirmed by numerical experiments. Our experiments with the pure advection problem also show that the Asselin filter does not seem to be helpful in improving the stability of the scheme for at least the pure advection computation if the necessary condition for stability is not met.

As we have seen in the numerical experiments, the CIP gives much better numerical solutions, but is more computationally expensive than the leapfrog scheme. It is interesting to compare the two schemes on an equalized basis in terms of computational cost, as in Bartello and Thomas (1996). We considered the advection of a one-dimensional cosine hill defined by

$$F = \frac{1 + \cos(r\pi)}{2}, \qquad r = \min\left(1, 2\frac{x - x_0}{a}\right),$$
$$a = 0.5, \qquad x_0 = 0.5, \qquad x \in [0, 1],$$

with a periodical boundary condition. Uniform grid spacing $\Delta x = 1/N$ and a constant Courant number CFL $= 0.5$ were used. In this particular test, we left out the Asselin filter to make the leapfrog method the most efficient. Since the initial profile is sufficiently smooth, the numerical dispersion of the leapfrog method seems to be tolerable even without the Asselin filter.

Both of the schemes were first run on the reference grid with $N = 100$ for 10 rounds (2000 steps). The elapsed time on a Pentium 1-GHz PC and the L_2 error (ε) are listed in Table 1. The L_2 error is computed by

$$\varepsilon = \frac{1}{N}\sum_{k=1}^{N}(f_k^\tau - F_k^\tau)^2,$$

for the τth time step, where f shows the numerical solution and F the exact one. As shown in Table 1, the CIP needs more than 3 times the elapsed time of the

TABLE 1. Comparisons of cost and accuracy between the CIP and the leapfrog methods. The CPU time is in units of s.

	CIP	Leapfrog			
	$N = 100$	$N = 100$	$N = 190$	$N = 300$	$N = 1000$
No. of steps	2000	2000	3800	6000	20 000
CPU time (s)	0.0321	0.0090	0.0323	0.0802	0.8911
ε	1.44×10^{-6}	4.67×10^{-3}	4.58×10^{-4}	8.73×10^{-5}	1.17×10^{-6}

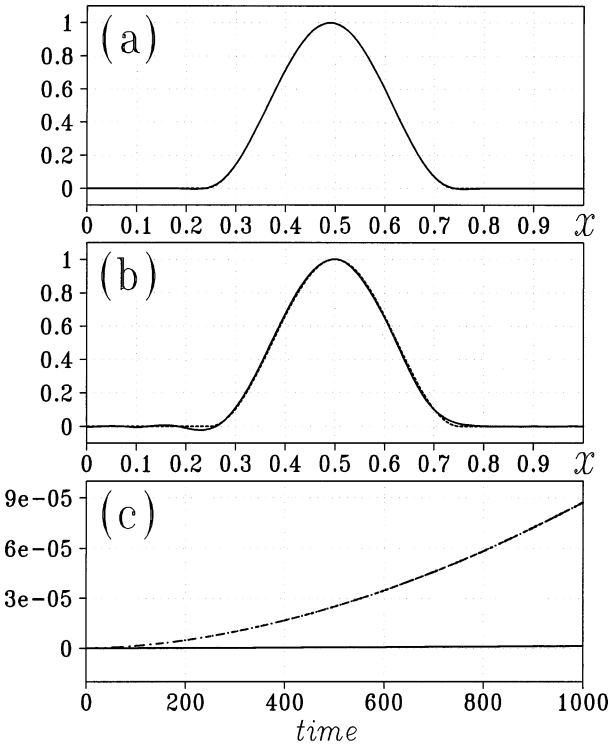

FIG. 4. One-dimensional advection of a cosine hill: (a) the CIP (solid, $N = 100$); (b) the leapfrog (solid, $N = 300$) after 10-cycle revolution, in comparing to the analytical result (dashed); and (c) L_2 errors of the CIP (solid) and the leapfrog (dashed).

leapfrog, but produced an L_2 error of less than 0.03% of the leapfrog. The grid was then refined gradually with $N = 190$, 300, and 1000 for the leapfrog computation. As expected, the numerical solutions of the leapfrog method were improved by the grid refinement. However, a finer grid spacing requires a smaller time integration interval and consequently more steps of calculation. We found that the computational time of the leapfrog method on a 190-point grid is equivalent to that of the CIP on the reference grid. The corresponding numerical error, however, is still far from comparable to that of the CIP reference computation. The results of the refined leapfrog ($N = 300$) and the reference CIP ($N = 100$) are illustrated in Figs. 4a and 4b along with the analytic solution, while the L_2 errors are plotted in Fig. 4c. Compared to the CIP, which accurately reproduced the exact solution, the dispersion error of the leapfrog is still obvious on the refined grids. Moreover, the numerical error of the leapfrog increases significantly with time. When the grid was refined tenfold, the L_2 error of the leapfrog method becomes less than for the CIP on the reference grid. However, with a tenfold-refined grid, the leapfrog needs much more CPU time than the CIP. Moreover, hightening the computational accuracy of advection by refining the mesh is not practical in real simulations where various physical processes are involved. We should note that when the profile is less smooth and has a large gradient, grid refinement cannot be always effective in improving the accuracy of the leapfrog method.

b. Real case simulations

The numerical results for advection are largely influenced by the computational scheme. As shown in section 3a, the results can be quite different from scheme to scheme, especially when the physical field contains small structures and large gradients. This issue may become serious for mesoscale storms, front systems, or small-scale vortex simulations, which are always associated with sharp spatial gradients and microscale perturbations. Further evaluation of the effect of advection computation and the comparison of the CIP with the leapfrog scheme for real case simulations are meaningful and necessary. In this subsection, the simulations of a continental rainstorm case (eastern China, June 1982) and a typhoon (no. 9810) case (Japan, October 1998) are presented. The comparisons between the numerical results computed, respectively, by the CIP method and the leapfrog method are discussed.

1) CASE 1

The first example is a severe rainstorm case over eastern China during 19~20 June 1982. Heavy rainfall was induced by mesoscale convective systems embedded in a shear line. Local precipitation reached 30 cm within 24 h. Both the CIP and the leapfrog methods are applied to simulate this case as the two options for advection computation in MM5 version 3.

(i) Simulation configuration and data

The computational mesh contains 80×80 horizontal grid points with a grid spacing of 40 km, and 23 σ levels. All σ levels are located at the same positions as mentioned in the last subsection. The domain center is at 32°N, 111°E. The top-level pressure of the model atmosphere is 100 hPa. A time step of 120 s is used. A simple ice scheme (Hsie et al. 1984) of an explicit moisture cycle, Grell-type (Grell 1993) cumulus parameterization, a Medium-Range Forecast (MRF, Hong and Pan 1996) model PBL parameterization scheme, and cloud radiation are adopted in this simulation.

National Meteorological Center (NMC, now NCEP) analysis data, which have horizontal resolutions of $2.5° \times 2.5°$ and 12 pressure levels, are used as the first-guess field. Initial data and boundary condition are produced via mesoscale objective analysis of rawinsonde data. Terrain and surface classification data with 30″ resolution were utilized for this region.

(ii) Numerical results

Two 24-h runs of that MM5, which were initiated at 1200 UTC 19 June 1982, are carried out with the leap-

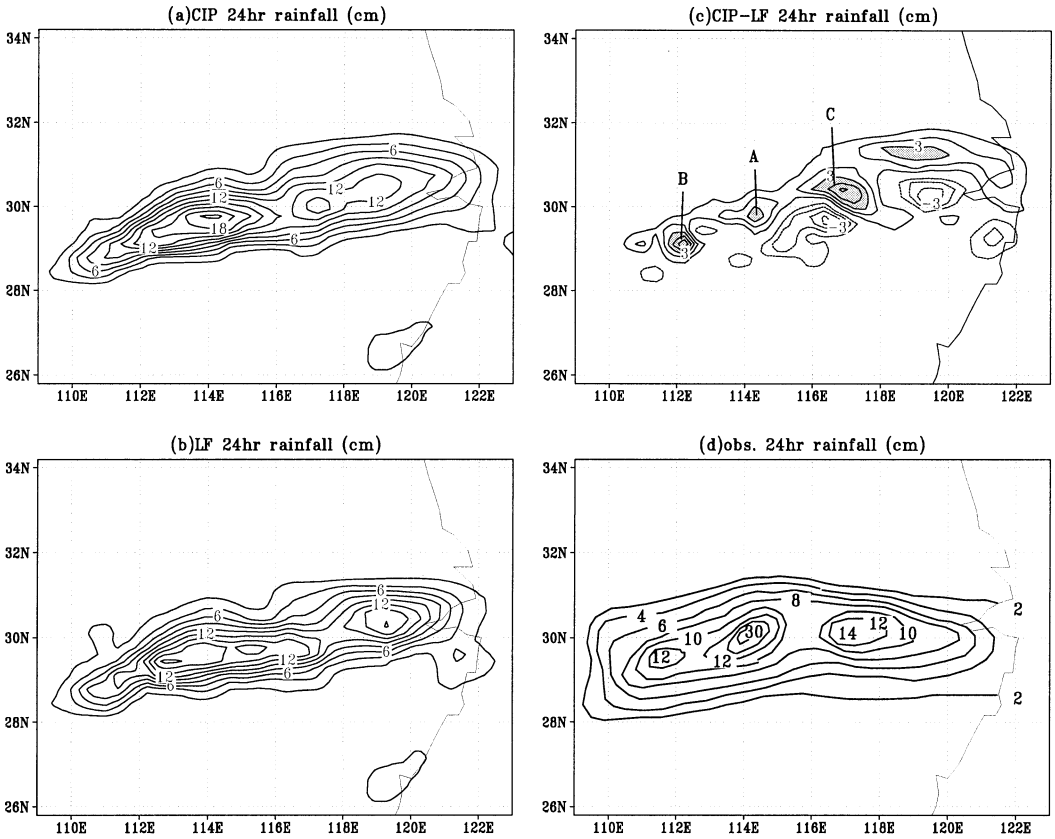

FIG. 5. The 24-h precipitation between 1200 UTC 19 Jun and 1200 UTC 20 June 1982, simulated with the (a) CIP and (b) leapfrog schemes, and (c) the difference between them in comparison with (d) the 24-h rainfall observation in case 1. Contour interval is 2 in (a) and (b), and 1 in (c). All panels are plotted in unit of cm.

frog and the CIP schemes, respectively. Simulated total rainfall, observed 24-h isohyet, and the difference in the model precipitation between the two schemes are presented in Fig. 5. Both schemes successfully simulated the rainband around 30°N, which has the same orientation as the observation (Fig. 5d). Several precipitation centers exist in the simulated rainband. In the CIP simulation, two peaks appear at 114° and 117°E, which correspond to the observation (Fig. 5d) very well. Although the area around 112°E is not isolated as a separated center, the 12-cm precipitation is of the same order as the observation. The contour of 14 cm is accurately simulated for the center at 117°E. Despite the maximum rainfall at 114°E in the CIP simulation being 20 cm, which is about 10 cm less than the local amount of the observation, it is still a better prediction than that of the leapfrog simulation. The simulation with the leapfrog method produced local maximum precipitation totals of 18, 16, and 14 cm at 112.7°, 115°, and 119°E within the rainband; neither the amount nor the position coincide with the observation. The rainfall difference between the CIP and the leapfrog (Fig. 5c) exhibits three evidently positive regions, which are labeled A, B, and C. The positive areas A, B, and C are located just at the positions where the observed peaks exist. This example reveals that the advection scheme can identify obvious differences in the rainfall from real simulation.

Let us examine the differences in the basic physical variables between the experiments with the two advection schemes for this real case. As illustrated in Fig. 6, the physical variables, like hourly rainfall, wind speed, pressure perturbation, and mixing ratio, of the CIP simulation evidently differ from those of the leapfrog simulation. At 2100 UTC 19 June, the difference in the hourly gridscale rainfall (Fig. 6a) at 30°N, 113.5°E shows its local maximum to be 1.0 cm. Two other peaks are also observed at 30°N, 116°E and 29°N, 112°E with values of 0.65 and 0.45 cm, respectively. The three positive peaks indicate that the CIP produced larger nonconvective rainfall at the locations where the three observed rainfall centers (Fig. 5d) are. We also find that the rainfall difference between the CIP and the leapfrog is basically concentrated within the strong shear zone in the low level (850 hPa). The sharp variation of wind results in the horizontal convergence of water vapor and other physical variables. Distinct wind speed variation between the two schemes is observed in the shear region with a large gradient as shown in Fig. 6b. Within the shaded area in Fig. 6b, the gradient of the wind speed is several times larger than in its neighboring area. The

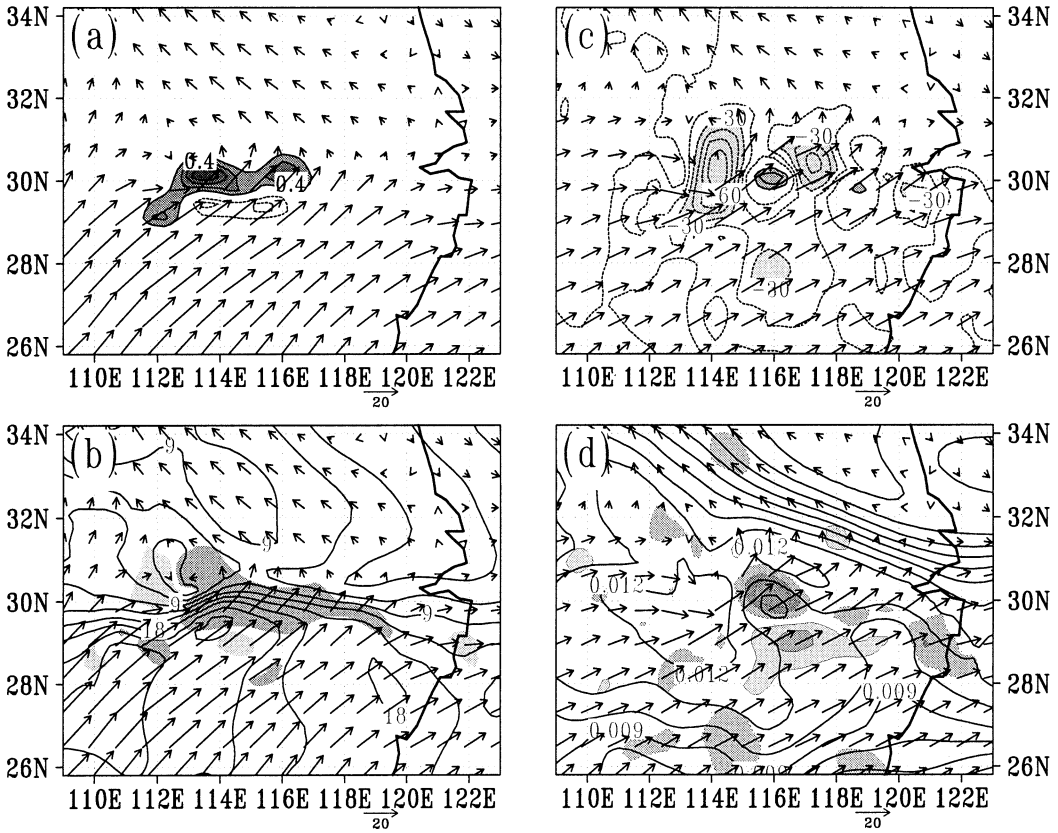

FIG. 6. Difference of (a) hourly gridscale rainfall (cm, positive is shaded) and (b) wind speed (shaded, m s^{-1}) between the CIP and leapfrog, in addition to wind speed itself [contour in (b), m s^{-1}] with the CIP, at 850 hPa of hour 9; (c) difference of pressure perturbation (Pa) and (d) mixing ratio difference (shaded, kg kg^{-1}), and mixing ratio (contour, kg kg^{-1}) at 700 hPa at hour 12 (0000 UTC 20 Jun) in case 1. Simultaneous horizontal wind vector in the CIP experiment is overlapped in all panels.

convergence of the horizontal wind tends to enhance the gradient. In this situation, the CIP can give reasonable results as the pure advection tests demonstrated in the last subsection.

At 700 hPa, the difference in pressure perturbation (Fig. 6c) mainly appears along 30°N (shaded areas) at 0000 UTC 20 June. Two negative centers are located at 114° and 117°E, while two positive centers are located at 116° and 119°E. This pattern has strong correlation with the simulated precipitation (Fig. 6a) and even with the 24-h rainfall as indicated by the peak value at the same position shown in Fig. 5. The mixing ratio of the water vapor (Fig. 6d) exhibits a large negative difference at the same position around (30°N, 116°E, which corresponds to the overestimation by the leapfrog method, and leads to the local large precipitation totals in the leapfrog experiment. The positive difference at 29°N, 116.5°E indicates that more vapor is transported there by the CIP. Meanwhile, no significant numerical diffusion occurred even in the vicinity of the local maximum center in the CIP simulation; thus, the vapor density is lower than that from the leapfrog simulation at 30°N, 116°E). As a result, no peak is observed around 116°E in the 24-h precipitation of the CIP simulation (shown in Fig. 5a). Because the CIP method can preserve the spatial distribution profile, the detail structures and thus the precipitation locations can be better simulated. As can be expected, although a large gradient of water vapor exists in the northern part of Fig. 6d, there is no obvious discrepancy between the simulations of the CIP and the leapfrog because of a weak wind field.

2) CASE 2

Typhoon Zeb (no. 9810) went passed over western Japan on 17 October 1998, with a maximum wind speed of 25 m s^{-1} and a center pressure of 975 hPa. Before it moved to the Sea of Japan at 1600 UTC 17 June (Fig. 7), heavy rainfall, flood, solifluction, and other serious disasters were brought to that area, especially to Okayama prefecture. A total loss of 63 billion Japanese yen was reported. During its passage over the land, rapid variation of local wind, dewpoint, and atmospheric pressure were observed in several locations. In Fig. 7, a typhoon cloud system, with strong convection, and a frontal cloud system are illustrated. The typhoon cloud covered a broad area. Due to the dynamical effects of

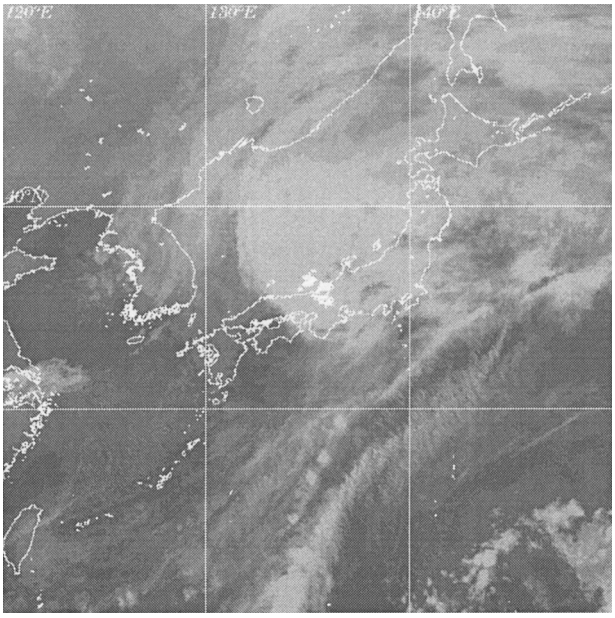

FIG. 7. *GMS-5* Visible Infrared Spin Scan Radiometer (VISSR) imagery at 1600 UTC 17 Oct 1998.

the land surface, its center pressure rose to 980 hPa when it crossed the Sea of Japan.

(i) Simulation configuration and data

The computational domain contains 150 × 150 horizontal grid points and 23 σ levels. The horizontal grid interval is 20 km. The domain is centered at 32°N, 131°E. The time step is specified as 40 s. The microphysical process and the PBL process are computed with the same schemes as in the previous case.

NCEP–NCAR global reanalysis data are used as model initial and boundary conditions, after horizontal and vertical interpolations. Original global data are distributed on 17 pressure levels and 2.5° × 2.5° latitude–longitude grids. Ten-minute resolution global terrain and land use data are interpolated to model grids.

(ii) Numerical results

Two 24-h simulations, initiating at 0000 UTC 17 October 1998, were carried out. As in the previous case, the impact of the two advection schemes is demonstrated by depicting the differences in the physical variables calculated by using the CIP and the leapfrog methods, respectively. In Fig. 8, the difference in hourly rainfall, pressure perturbation, mixing ratio, and vertical velocity (w) at hour 16 (1600 UTC 17 October) are exhibited. The wind field on the lowest σ level from the CIP simulation is also plotted, so that the position of the typhoon can be easily recognized. In Fig. 8a, the rainfall difference between the simulations with the two advection schemes varies from −2.6 to 2.4 cm in the typhoon and the frontal region. Though surface pressure perturbation is deformed largely by the dynamic effects of topography, the vertical flow is perfectly simulated by both schemes. The storm center is predicted at 36°N, 134°E by the CIP, which is in agreement with the weather chart (not shown here) and the satellite image (Fig. 7). In the cyclonic circulation, a positive region of rainfall difference is located ahead of the negative one, which means that the rainband was transported more slowly by the leapfrog than the CIP. It can be attributed to the significant dispersion error of the leapfrog for large gradient transportation. Two remarkable regions are also observed in the difference of the pressure perturbation (Fig. 8b). The negative one, which shows lower pressure in the CIP simulation, lies in the central area of the storm; and the positive one lies to the south of the typhoon core. The minimum pressure in the CIP simulation is 200 Pa lower than that of the leapfrog simulation in the typhoon region. On the other hand, the leapfrog method produced lower pressure over the shear line. In Fig. 8c, the difference in the mixing ratio is distributed meridionally, just like the hourly rainfall in Fig. 8a, where strong wind shear and a large mixing ratio gradient existed. It is obvious that a large difference in the water vapor transportation between the CIP and the leapfrog exists in the area associated with strong wind shear and the spatial gradient of the mixing ratio. A similar distribution of the vertical velocity difference at the middle level is found in Fig. 8d. In the confluence flow of the shear line, departure of vertical velocity shows a faster eastward movement of the shear line in the CIP simulation. Different peaks and vertical structure are produced by the two schemes.

In Fig. 9, averaged surface pressure, u component, and temperature over a 20 km × 20 km area in Okayama are presented in comparison with the base observation of surface pressure and temperature. Though simulated surface pressure did not vary as rapidly as the observation, the appearance of the minimum pressure of 978 hPa during 1400–1500 UTC is accurately predicted in the CIP simulation. In the leapfrog experiment, the surface pressure reached its minimum value at 1500 UTC, but another weak local minimum appeared 2 h earlier at 1300 UTC.

The observed u component of the surface wind turned during 1300–1400 UTC, which coincided with the simulated variation of surface pressure. In fact, the surface u component changed direction during 1400–1500 UTC in the CIP experiment when the typhoon went through Okayama. At the same time the surface pressure reached its minimum in the CIP experiment. This agrees well with the observation, as shown in Fig. 9b. But the location of the typhoon in the leapfrog experiment is different. A pressure dip is observed at 1515 UTC (Fig. 9b); however, neither numerical experiment was able to reproduce it. The abrupt descents in temperature and dewpoint observed around 1500 UTC were correctly described by the numerical experiments with the two

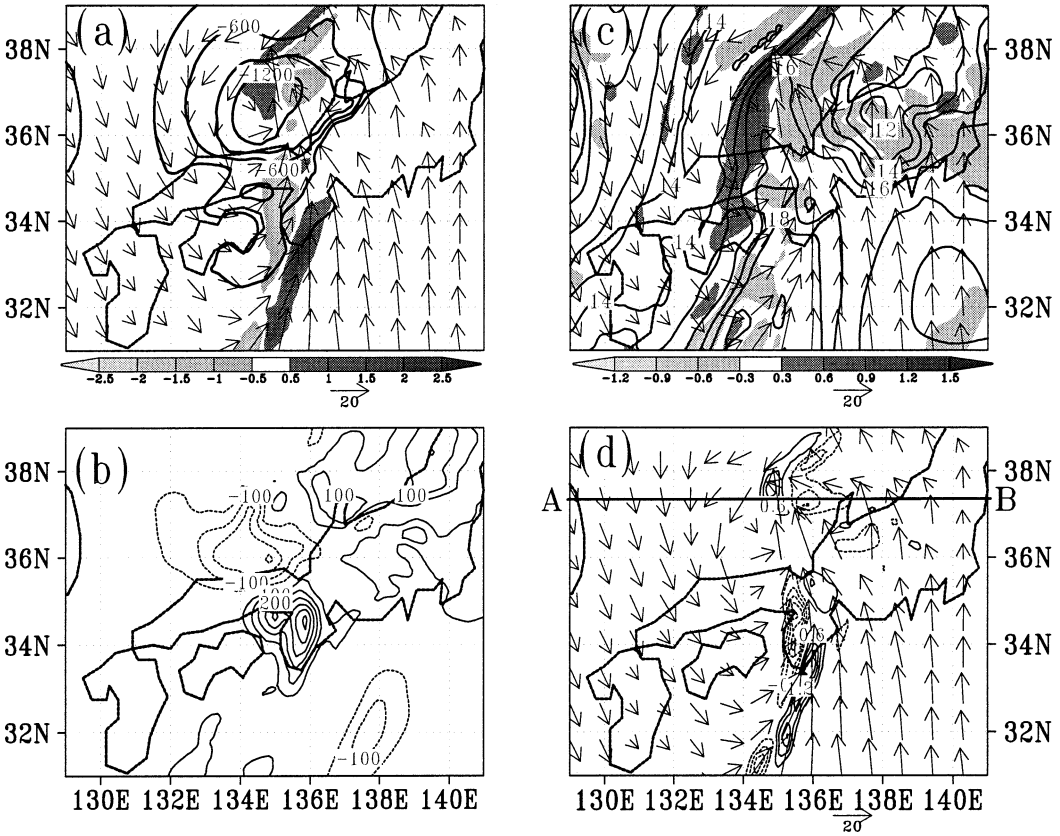

FIG. 8. (a) Pressure perturbation (thick solid, Pa) and difference of hourly rainfall (shaded, cm) between the CIP and leapfrog (same in other panels) schemes; (b) pressure perturbation difference (thin contour) and (c) mixing ratio and the difference (g kg^{-1}, shaded) at the lowest σ level; (d) difference of midlevel vertical velocity w (m s^{-1}) at σ = 0.575 by hour 16. Vectors show the wind on the lowest model level of σ = 0.995 in the CIP experiment. Line AB in (d) is the location of the vertical cross section in Fig. 10.

schemes. The sudden declination in the observed surface temperature at 1500 UTC was accurately captured by the CIP simulation, while a slack descent was produced at 1300 UTC in the leapfrog experiment, though the steep descent happened during 1600–1900 UTC. The CIP simulation appears to be considerably more favorable in reproducing the details of the physical process.

The typhoon is characterized by extremely strong convection, and the vertical velocity experiences violent changes within a relatively narrow area. The simulated

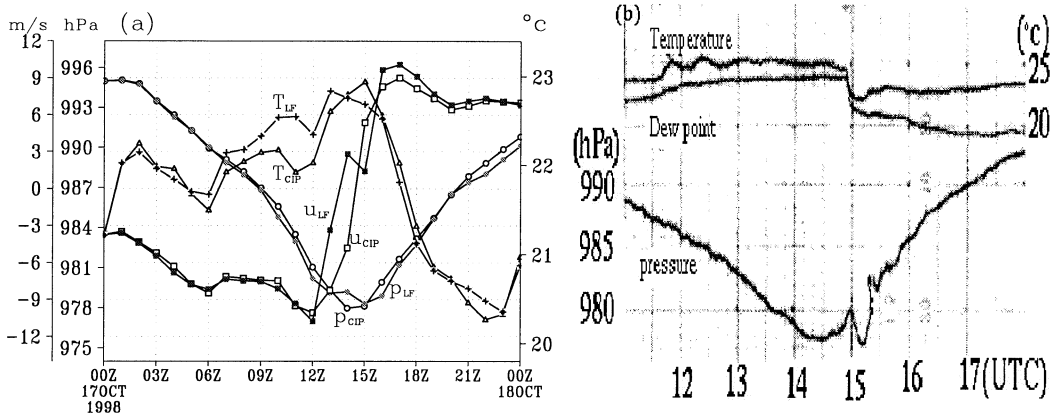

FIG. 9. Evolution of (a) simulated surface pressure (hPa), u component (m s^{-1}), and temperature (°C) in the CIP and the leapfrog experiments; (b) observed surface pressure (hPa), temperature (°C), and dewpoint (°C) at Okayama.

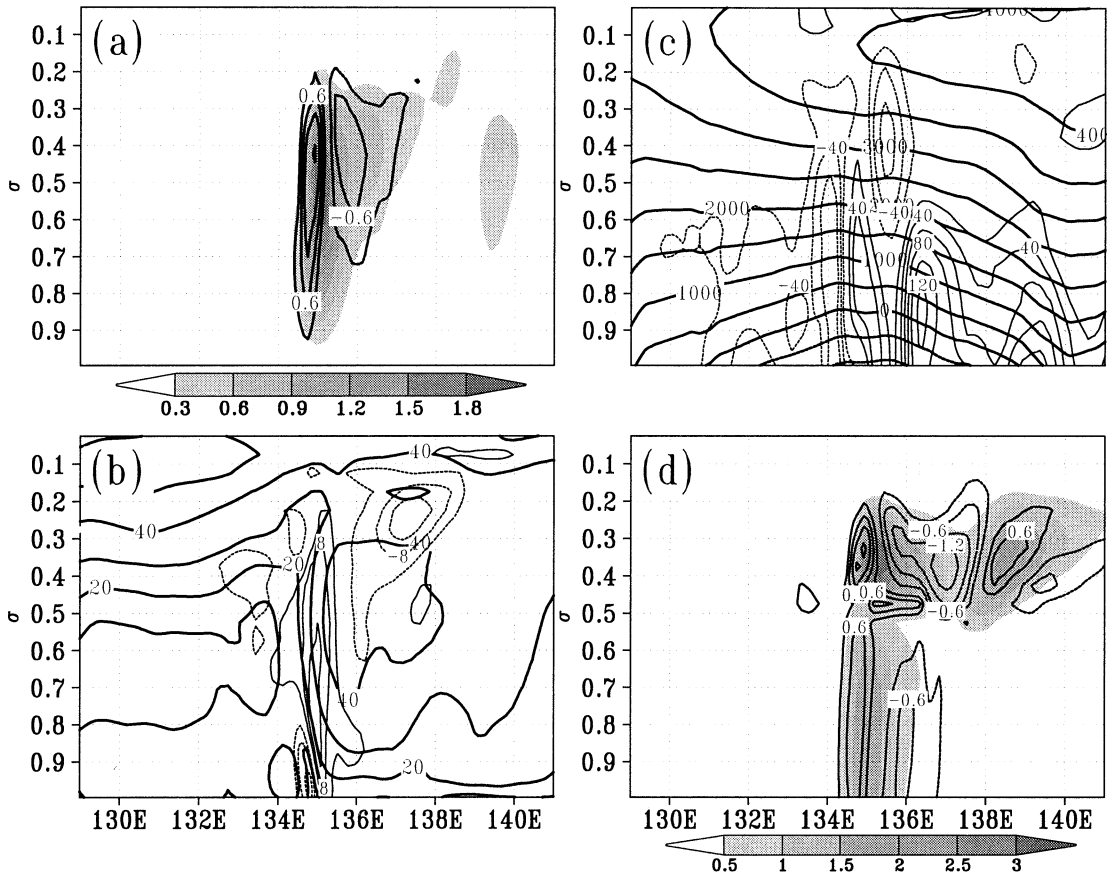

FIG. 10. Vertical cross section of (a) vertical velocity w (shaded, m s^{-1}), (b) horizontal wind speed (thick, m s^{-1}), (c) pressure perturbation (thick, Pa), and (d) rainwater (shaded, g kg^{-1}) simulated with CIP, in addition to the difference (thin contour) between the CIP and leapfrog, at 1600 UTC 17 Oct along 37.5°N (AB in Fig. 8d), where the maximum vertical ascent is located.

vertical structure of the typhoon will be substantially affected by the advection scheme in numerical prediction. A vertical cross section of some of the physical variables is plotted in Fig. 10, along AB in Fig. 8d. Differences in vertical velocity between simulations with the CIP and the leapfrog show basically a vertically uniform distribution in Fig. 10a, where a strong horizontal wind gradient and convergence are observed. The maximum gets to 1.2 m s^{-1} on $\sigma = 0.45$. In both experiments, the vertical velocity w itself is also distributed uniformly in the vertical direction of the midlevel atmosphere. This mainly shows the effect of strong vertical advection. Horizontal wind speed was transported by the vertical current within the convective region, which resulted in a vertically uniform distribution and a horizontally sharp variation (Fig. 10b).

Large differences between the CIP and the leapfrog simulations concentrate in the horizontal shear area. Pressure perturbations and rainwater also show the same pattern in the lower troposphere. At upper levels ($\sigma =$ 0.2 to 0.4), the difference of the rainwater looks more complex. This may be owed to the integral effects of dynamical and physical processes, such as advection, diffusion, cumulus parameterization, etc. Generally, numerical transport varied greatly between the two schemes within the shear region, where a strong horizontal gradient and a sharp wind convergence exist.

4. Summary

We have adopted an HV splitting scheme of the CIP to the advection computation in the MM5. The resulting scheme has accuracy of third order in space and second order in time. The time integration formulation and all the numerical aspects except the advection scheme are retained as they are in the original MM5 model. We tested the modified model with pure advection experiments.

Being an advection scheme, the CIP appears to be far superior to the original leapfrog scheme in simulating discontinuous distribution. Real case studies reveal that with the CIP being the advection solver the detail structures can be more reasonably simulated by the MM5 model. The superiority of the CIP becomes more prominent in the advection dominant process with large gradients in the advected field. Since mesoscale severe

weather systems are always associated with drastic changes and large gradients in various physical fields, more attention should be paid to the advection computation in the high-resolution simulations for these phenomena.

As a semi-Lagrangian-type scheme, the CIP can be computationally stable even with a large Courant number, though using large CFL numbers may cause relatively large numerical errors as reported in some literature. In a meteorological model, like MM5, various modes and physical processes are involved, so even in the CIP simulations we still used CFL numbers of less than unity. Further work is needed before we can take full advantage of semi-Lagrangian schemes and implement large CFL simulations to improve the computational efficiency.

Acknowledgments. The authors would like to thank Prof. T. Aoki of the Tokyo Institute of Technology and Dr. T. Utsumi of the Japan Atomic Energy Research Institute for their helpful suggestions and useful discussions, as well as two anonymous reviewers for their valuable suggestions on improving this paper. Thanks are also given to Prof. S. Lu in the Cold and Arid Region Environmental and Engineering Research Institute, Chinese Academy of Science, and to Dr. C. Liu of NCAR for their help with the dataset. This work was supported by NASDA, Japan.

REFERENCES

Anthes, R. A., 1977: A cumulus parameterization scheme utilizing a one-dimensional cloud model. *Mon. Wea. Rev.,* **105,** 270–286.

Bartello, P., and S. J. Thomas, 1996: The cost effectiveness of semi-Lagrangian advection. *Mon. Wea. Rev.,* **124,** 2883–2897.

Carpenter, R. L., K. K. Droegemeier, P. R. Woodward, and C. E. Hane, 1990: Application of the piecewise parabolic method (PPM) to meteorological modeling. *Mon. Wea. Rev.,* **118,** 586–612.

Colella, P., and P. R. Woodward, 1984: The piecewise parabolic method (PPM) for gas-dynamical simulations. *J. Comput. Phys.,* **54,** 174–201.

Dudhia, J., 1993: A nonhydrostatic version of the Penn State/NCAR mesoscale model: Validation tests and simulation of an Atlantic cyclone and cold front. *Mon. Wea. Rev.,* **121,** 1493–1513.

Grell, G. A., 1993: Prognostic evaluation of assumptions used by cumulus parameterizations. *Mon. Wea. Rev.,* **121,** 764–787.

Harten, A., 1983: High resolution schemes for hyperbolic conservation laws. *J. Comput. Phys.,* **49,** 357–393.

Hong, S.-Y., and H.-L. Pan, 1996: Nonlocal boundary layer vertical diffusion in a medium-range forecast model. *Mon. Wea. Rev.,* **124,** 2322–2339.

Hsie, E.-Y., R. A. Anthes, and D. Keyser, 1984: Numerical simulation of frontogenesis in a moist atmosphere. *J. Atmos. Sci.,* **41,** 2581–2593.

Staniforth, A., and J. Côté, 1991: Semi-Lagrangian integration scheme for atmospheric model—A review. *Mon. Wea. Rev.,* **119,** 2206–2223.

Tanaka, R., T. Nakamura, T. Yabe, and H. Wu, 1999: A class of constructing formulation of the CIP method. *Comput. Fluid Dyn. J.,* **8,** 1–5.

van Leer, B., 1977: Toward the ultimate conservative difference scheme. IV. A new approach to numerical convection. *J. Comput. Phys.,* **23,** 276–299.

——, 1979: Toward the ultimate conservative difference scheme. V. A second-order sequel to Godunov's method. *J. Comput. Phys.,* **32,** 101–136.

Xiao, F., T. Yabe, and T. Ito, 1996: Constructing oscillation preventing scheme for advection equation by rational function. *Comput. Phys. Commun.,* **93,** 1–12.

Yabe, T., and T. Aoki, 1991: A universal solver for hyperbolic-equations by cubic-polynomial interpolation. I. One-dimensional solver. *Comput. Phys. Commun.,* **66,** 219–232.

——, T. Ishikawa, P. Y. Wang, T. Aoki, Y. Kodota, and F. Ikeda, 1991: A universal solver for hyperbolic-equations by cubic-polynomial interpolation. II. Two- and three-dimensional solvers. *Comput. Phys. Commun.,* **66,** 233–242.

——, R. Tanaka, T. Nakamura, and F. Xiao, 2001: An exactly conservative semi-Lagrangian scheme (CIP-CSL) in one dimension. *Mon. Wea. Rev.,* **129,** 332–344.